Mechanistic modeling of the thermal-hydraulics in polydispersed flow film boiling in LOCA conditions

A.V.S. Oliveira, J.D. Peña Carrillo, Alexandre Labergue, T. Glantz, Michel Gradeck

Mechanistic modeling of the thermal-hydraulics in polydispersed flow film boiling in LOCA conditions

A.V.S. Oliveira[a,b,*], J.D. Peña Carrillo[a,b], A. Labergue[a], T. Glantz[b], M. Gradeck[a]

[a] *LEMTA, UMR CNRS 7563, Université de Lorraine, Vandoeuvre-Lès-Nancy 54505, France*
[b] *IRSN, PSN/SEMIA/LIMAR, B.P. 3, 13115 Saint Paul-Lez-Durance, France*

Abstract

Much effort has been devoted by the nuclear community to develop mechanistic models to predict the heat dissipation of fuel rods during a loss of coolant accident (LOCA). However, there is still the challenge to find correlations that accurately predict the rates of heat transfer corresponding to each involved phenomena and gather them all in a single physical model. Looking for improving thermal-hydraulics calculations in LOCA conditions, this work introduces a novel mechanistic model implemented in a new code named NECTAR to calculate heat and mass transfer phenomena and droplets dynamics in a polydispersed flow film boiling. The simulation results are compared with experimental measurements using three different geometries that represent the cladding ballooning at sub-channel scale. NECTAR can predict with great accuracy the heat dissipation by the internal steam-droplets flow with less than 8% mean deviation for all the test cases. The droplets characteristics downstream of the heated tube are also well predicted by NECTAR. In a detailed analysis of each heat transfer process, we found that wall-to-steam convection plays the major role in the internal heat dissipation, followed by the heat removed by the droplets impact onto the wall in spite of the very low volume fraction of droplets. Moreover, droplets impact and steam-to-droplets convection are also the main responsible for the droplets evaporation. Finally, considering the droplets diameter polydispersed distribution into thermal-hydraulics calculations (instead of a single mean diameter) has an effect only for higher volume fractions of droplets.

Keywords:
NECTAR, LOCA, Thermal-hydraulics, Mechanistic model, Polydispersed distribution

Nomenclature

Greek letters

α	volume fraction	ω	coalescence and breakup term
ϵ	emissivity	Φ	rate of heat flow
η	order of the moment	ρ	density
γ	surface tension	σ	log-normal standard deviation
μ	log-normal mean	σ_{SB}	Stephan-Boltzmann constant
		τ_b	blockage ratio

*Corresponding author
Email address: vieradas1@univ-lorraine.fr (A.V.S. Oliveira)

φ	heat flux
ϑ	drag coefficient correction

Roman letters

$\dot{m}$	mass flow rate
A	cross-sectional area
a_i	interfacial area concentration
B	Spalding factor
Bi	Biot number
C	drag coefficient
c_p	specific heat
D	diameter (tube)
d	diameter (droplets)
E	energy
f_f	friction factor
G	change in droplets diameter
g	acceleration of gravity
h	heat transfer coefficient
h_{ls}	heat of vaporization
L	length
m	mass
n	density of droplets
Nu	Nusselt number
P	droplets diameter distribution
Pr	Prandtl number
r	radial direction
Re	Reynolds number
S	moment
T	temperature
t	time
u	axial velocity
We	Weber number
z	axial position

Subscripts

32	Sauter mean diameter
b	blockage
c	convection
d	droplets
ev	evaporation
ext	external
imp	droplets impact onto the wall
int	internal
j	bin number
loss	heat losses
low	bin's lower limit
R	residence period
r	radiation
s	steam
t	tube
up	bin's upper limit
w	wall

1. Introduction

Detailing the heat transfer phenomena during the reflooding phase of a loss of coolant accident (LOCA) is still a challenging task although much effort has been devoted to this subject in the last two decades [1]. Multidimensional thermal-hydraulics and advanced mechanistic physical models are highly studied by the nuclear community to improve the safety of reactor cores, in both experimental and numerical approaches [2–8]. This dedication is justified by the complex conjugated phenomena taking place during the reflooding phase in a LOCA.

Figure 1 shows the different heat transfer processes and fluid dynamics characteristics depending on the position in the fuel rods from the quenching front. Nucleate boiling is the main heat transfer path on rods immersed in water. Meanwhile, immediately downstream of the quenching front, the fuel rods are firstly cooled down by a dispersed steam-droplets two-phase flow. Early during reflood when the water level is low, there is no liquid entrainment and the generated droplets are evaporated in the length of the fuel rods bundle [9, 10], leading to heat transfer by convection with superheated steam. Since the two-phase flow plays an important role in the heat dissipation of the upper part in the nuclear core, evaluating the rate of heat transfer in this region is essential. However, this is also a difficult exercise because of the many different processes taking place. Examples are: turbulent flow; droplets formation at the quenching front and their later coalescence and fragmentation in the steam flow; droplets impact onto heated walls; radiative heat transfer; and geometrical effects due to the fuel claddings ballooning and burst. Only a thorough mechanistic model can accurately predict the heat dissipation and the coolability of the fuel rods and, by consequence, give confidence in nuclear safety in LOCA conditions.

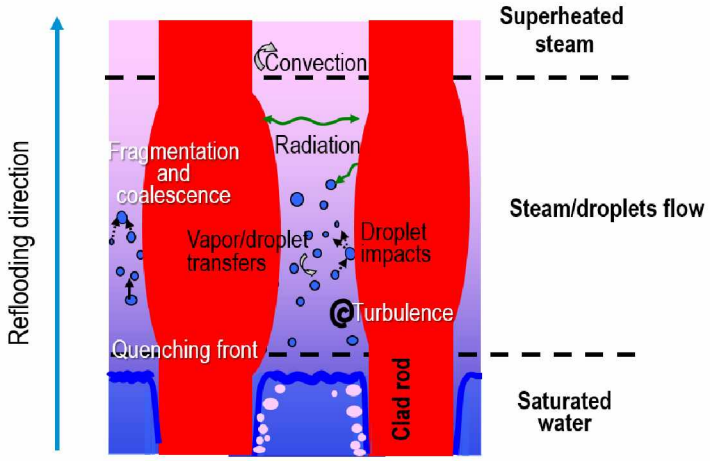

Figure 1: Heat and mass transfer phenomena during LOCA.

Several authors have already proposed different mechanistic models for the post-dryout heat transfer with an internal steam-droplets flow. One of the firsts was proposed by Sun et al. [11], where they considered convection and radiation between the three participants (wall, steam and droplets) but without droplets impact onto the wall. Guo and Mishima [12] later included more phenomena in the calculations, like droplet impact onto heated walls and evaporation using a mean droplet diameter, and evaluated the importance of each heat transfer path in the cooling of the heated wall. Meholic et al. [13] presented a 2-D model where, for instance, they analyzed the effect of the droplet size and wall temperature on the impact of the droplet onto the wall. More recent examples are available in the literature, including one-dimensional modeling [14] and the use of a computational fluid dynamics code [15].

However, accurate physical models are still a challenge to describe the thermal-hydraulics during the cooling phase in LOCA conditions. Thus, the Institut de Radioprotection et de Sûreté Nucléaire (IRSN), in France, launched the project PERFROI [16]. One objective among others is to increase the understanding of the thermal hydraulic phenomena during the cooling phase to better predict the coolability of a nuclear core, especially with ballooning

of claddings. With this perspective, this work presents a new code called NECTAR [1] using a mechanistic model that estimates both the heat dissipation by the internal steam-droplets flow in LOCA conditions and the droplets characteristics (diameter and velocity) in a polydispersed distribution. We compare the results of this code with experimental data obtained from COLIBRI [2], an experimental rig dedicated to the thorough investigation of the thermal-hydraulics during the cooling of a vertical pipe with an internal mist flow. We also compare the predictive capacity of NECTAR with IRSN's code DRACCAR, which is a 3D multiphysics simulation tool to investigate, among other problems, the thermal-mechanical and thermal-hydraulics of a nuclear core during LOCA transients. Detailed information concerning the code DRACCAR is available in a two-part paper with a general description of the modeling [2] and its simulation capability [3].

2. COLIBRI: experimental apparatus

As the objective of this paper is to introduce the thermal-hydraulics modeling with NECTAR, the presentation of the experimental apparatus dedicated to its validation is herein summarized. The detailed information regarding the test bench and measurement techniques is available in previous works [17, 18].

Figure 2 presents a schematic illustration of COLIBRI. The test section, made of Inconel-625, is divided into three parts. Parts I and III are fixed tubes with an internal diameter of 11.78 mm and a thickness of 0.57 mm, which is representative of a fluid sub-channel in a Pressurized Water Reactor (PWR). The supply systems of droplets and steam converge at the mixer upstream of Part I to provide the dispersed two-phase flow to the test section. Part II is heated by Joule effect with the aid of a direct-current power source and is removable to allow testing different blockage ratios τ_b by reducing the tube internal diameter D_{int}. The blockage ratio is calculated by:

$$\tau_b = 1 - \left(\frac{D_{int}}{0.01178}\right)^2 \tag{1}$$

and indicates the constriction level in Part II, being 0% if the internal diameter is 11.78 mm (as in Parts I and III) and 100% if it is zero.

Upstream and downstream of Part II, there are optical windows for measurements of the droplets axial velocity (the z-component) and diameter using a typical phase-Doppler analyzer (PDA) and of the mean droplets temperature using three-color laser induced fluorescence (3cLIF) thermometry. One great advantage of 3cLIF is the capability of correcting the droplet size effect on the temperature measurement, as described in Labergue et al [19]. Meanwhile, we used infrared thermometry (IRT) to measure the temperature profile of the external surface of Part II during the cooling phase.

Table 1 shows the Part II geometries we tested to analyze the blockage ratio effect on the cooling process and to validate the code NECTAR. We should note that the wall thickness at the constriction of the tube is different for each configuration to ensure that we would have Part II with similar masses and, by consequence, similar thermal inertia. This allows us to evaluate separately the blockage ratio effect on the thermal-hydraulics of the cooling phase, although in a real LOCA condition the cladding becomes thinner with the ballooning, reducing its linear thermal

[1] **N**ew **E**xperimental **C**ode for **T**hermal-hydraulic **A**nalysis in a **R**epresentative geometry

[2] **CO**o**LI**ng of **B**lockage **R**egion **I**nside a PWR Reactor

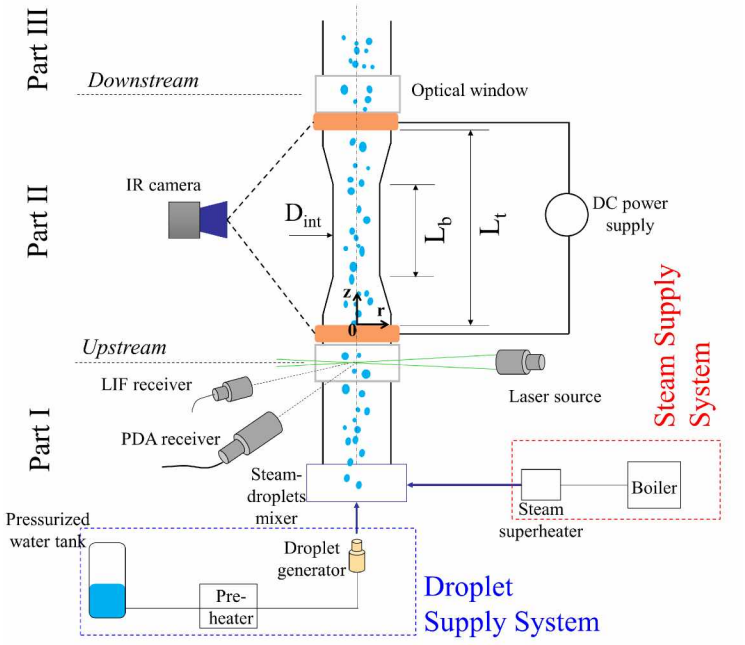

Figure 2: Experimental apparatus COLIBRI.

inertia [20]. Moreover, conserving the same cross-sectional area results in a constant linear electrical resistance and a uniform heat generation by Joule effect, which results in a nearly uniform axial temperature on the tube surface before the cooling experiment.

Table 1: Configurations of the test section (Part II)

Configuration	**1**	**2**	**3**
Blockage ratio (τ_b)	0%	61%	90%
Internal diameter (D_{int})	11.78 mm	7.35 mm	3.72 mm
Blockage length (L_b)	-	100 mm	100 mm
Length between contacts (L_t)	175 mm	140 mm	175 mm
Wall thickness	0.57 mm	0.95 mm	1.45 mm

The experimental procedure is the following: first, we start the steam supply system and let it flowing for about 40 minutes to heat the supply system and the test section. Then, we start both the droplets injection and the DC power supply until Part II reaches a temperature of approximately 600 °C. Once reached steady-state condition, we used the PDA system upstream of Part II for the droplets diameter and velocity measurements, and the 3cLIF thermometry up- and downstream of Part II to measure the mean droplets temperature. Finally, we turned off the DC power supply to start the cooling process, performing simultaneous and synchronized IRT and PDA measurements. Table 2 summarizes the ranges used in the present experiments, showing that they are representative of a typical LOCA condition. Note that, compared to LOCA values, the steam temperature is in the lower range. In a real

scenario, steam temperatures slightly higher than saturation is representative of the near field, the region close to the quenching front [9].

Table 2: Typical values during LOCA and those obtained with COLIBRI upstream of Part II

Parameter	**Typical LOCA values [6, 7, 9, 21]**	**COLIBRI (upstream of Part II)**
Droplets diameter (d_d)	50 μm – 1000 μm	5 μm – 300 μm
Droplets axial velocity (u_d)	4 m/s – 16 m/s	13 m/s – 16 m/s
Volume fraction of droplets (α_d)	10^{-2} – 10^{-4}	$\approx 10^{-4}$
Steam temperature (T_s)	Up to 800 °C	160 °C – 170 °C
Wall temperature (T_w)	300 °C – 1200 °C	300 °C – 600 °C

Using the spatial-temporal decrease of the tube temperature T_w measured with the IRT and considering azimuthal symmetry, we can estimate the heat dissipation by the internal two-phase flow φ_{int} with the following energy balance equation:

$$\varphi_{int}(z,t) = -\left(\frac{A_t \rho_w c_{p,w}}{\pi D_{int}}\right)\frac{dT_w(z,t)}{dt} - \left(\frac{D_{ext}}{D_{int}}\right)\varphi_{loss}(z,t) \tag{2}$$

where A_t, ρ_w, $c_{p,w}$, D_{int}, and D_{ext} are, respectively, the cross-sectional area, the density, the specific heat capacity, the internal diameter, and the external diameter of the test section, while φ_{loss} is the sum of the heat losses to the ambient by radiation and convection.

The experimental uncertainties either found by error propagation and repetitive measurements are:

- Wall temperature (IRT): ±5 °C;
- Internal heat flux (Eq. 2): ±10%;
- Droplets velocity (PDA): ±5%;
- Droplets diameter (PDA): ±10%;
- Droplets temperature (3cLIF): ±5 °C.

3. NECTAR: code presentation

3.1. General description and hypotheses

Guo and Mishima [12] presented in their work a simplified mechanistic approach to estimate the heat and mass transfer processes taking place in a dispersed flow film boiling. Following their strategy, NECTAR considers the main thermal-hydraulics parameters of the two-phase flow and calculates the heat transfer paths as shown in Fig. 3, being:

- $\Phi_{c,ws}$: wall-to-steam convection;
- $\Phi_{r,ws}$: wall-to-steam radiation;
- $\Phi_{c,sd}$: steam-to-droplets convection;
- $\Phi_{r,sd}$: steam-to-droplets radiation;
- $\Phi_{r,wd}$: wall-to-droplets radiation;
- $\Phi_{imp,wd}$: wall-to-droplets direct impact;
- and $\dot{m}_{ev}$: evaporation rate of droplets.

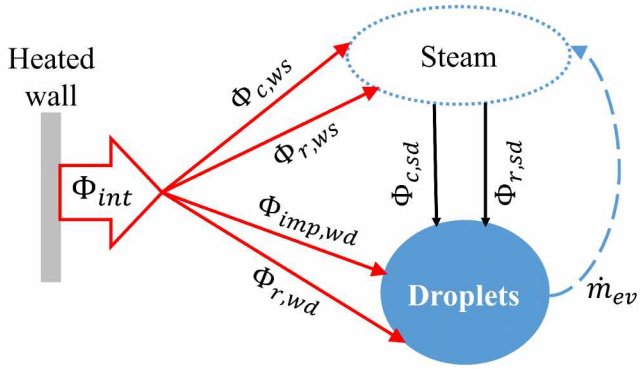

Figure 3: Heat transfer paths considered in NECTAR, as proposed by Guo and Mishima [12].

Although NECTAR estimates all the heat transfer paths and they all affect the thermal-hydraulics of the cooling process, we should notice that only $\Phi_{c,ws}$, $\Phi_{r,ws}$, $\Phi_{r,wd}$, and $\Phi_{imp,wd}$ directly contributes to the wall heat dissipation Φ_{int}, which means:

$$\Phi_{int} = \Phi_{c,ws} + \Phi_{r,ws} + \Phi_{r,wd} + \Phi_{imp,wd} \tag{3}$$

The general hypotheses made in NECTAR are the following:

1. 1-D (axial) two-fluid model (steam and droplets) in thermal and dynamic non-equilibrium;
2. Droplets are spherical and at saturation temperature, as experimentally verified [17];
3. No droplets coalescence, although droplets breakup is considered;
4. No wall separation of the dynamic boundary layer due to geometrical expansions (in the case of deformed tubes);
5. The wall is thermally thin (Bi $\ll 1$ for all the experiences), hence there is no temperature gradient in the radial direction of the tube;
6. Wall rewetting is not considered, hence the code is only valid for the Leidenfrost regime.

Although it seems similar to the model proposed by Guo and Mishima, NECTAR adopts different methods and correlations, as we explain throughout the next sections.

3.2. Conservation equations

The droplets diameter decreases along the flow because of evaporation and, consequently, there is an increase in the mass of steam. This process is described by a mass conservation equation as follows:

$$\frac{dm_s}{dt} = \dot{m}_{ev} \tag{4}$$

where dm_s/dt is the rate of change in the mass of steam and $\dot{m}_{ev}$ is the evaporation rate of the droplets.

The main forces acting on the droplets are weight and drag by the steam. Other forces like lift, added mass, and near-wall evaporation are neglected in the present model. Hence, the momentum conservation equation in the z-direction (axial) for the droplets is:

$$\rho_d u_d \frac{du_d}{dz} = -\frac{3}{4d_d}\frac{\vartheta C_d}{1+B}\rho_s \left(u_d - u_s\right)\left|u_d - u_s\right| + \left(\rho_s - \rho_d\right) g \tag{5}$$

where ρ, u and d are, in this order, density, axial velocity and diameter. The subscripts s and d stand for steam and droplets, respectively. The drag coefficient C_d is calculated with Morsi's correlation as a function of the droplets Reynolds number [22] and it is reduced by the factor $1/(1+B)$ (B being the thermal Spalding factor [23]) due to the droplets evaporation. Furthermore, ϑ is a coefficient that considers the influence of the droplet volumetric concentration α_d in the calculation of C_d, expressed by:

$$\vartheta = \frac{1}{1 - 6.55\alpha_d} \tag{6}$$

Finally, energy balance equations are applied on every differential element dz to evaluate the change in the steam temperature and the evaporated mass along the tube length. Considering the heat exchange on the steam presented in Fig. 3, we can find the following equation for the steam temperature downstream of a differential element at z:

$$T_s\left(z + dz\right) = \frac{\left[\Phi_{c,ws} + \Phi_{r,ws} - \Phi_{c,sd} - \Phi_{r,sd}\right] + \dot{m}_s(z) c_{p,s} T_s(z)}{\left[\dot{m}_s(z) + \frac{dm_s}{dt}(z)\right] c_{p,s}} \tag{7}$$

Similarly, an energy balance equation is also necessary to estimate the evaporated mass of droplets at a differential element at z (Fig. 3), so:

$$\dot{m}_{ev} = \frac{\Phi_{ev}}{h_{ls}} = \frac{\Phi_{c,sd} + \Phi_{r,sd} + \Phi_{r,wd} + \Phi_{imp,wd}}{h_{ls}} \tag{8}$$

where Φ_{ev} represents the sum of all the rates of heat transfer on the droplets and h_{ls} the heat of vaporization of water.

3.3. Empirical correlations

To estimate the rates of heat transfer present in Eqs. 3, 7 and 8, we used empirical correlations available in the literature. Table 3 presents the ones used in NECTAR.

Two heat transfer paths are calculated differently from the model by Guo and Mishima [12]. The first is for the wall-to-steam convection ($\Phi_{c,ws}$), which has lots of correlations available in the literature. We chose the Gnielinski's correlation because it presented great match with our experimental data with a steam monophasic flow, as we present in the results section. The second different one is the heat dissipation by droplets impact onto the heated

Table 3: Empirical correlations used in the present work

PARAMETER		CORRELATION
$\Phi_{c,ws}$	Gnielinski [24]	$Nu_s = \frac{\left(\frac{f_f}{8}\right)(Re_s - 1000)Pr}{1+17\left(\frac{f_f}{8}\right)^{0.5}\left(Pr^{\frac{2}{3}}-1\right)}\left(\frac{T_s}{T_w}\right)^{0.14}$
$\Phi_{c,sd}$	Lee and Ryley [25]	$Nu_d = \frac{2+0.74Re_{sd}^{0.5}Pr^{0.33}}{1+B}$
$\Phi_{r,ws}$,$\Phi_{r,wd}$ and $\Phi_{r,sd}$	Sun et al. [11]	Thermal resistance circuit (Y-Δ transform)
$\Phi_{imp,wd}$	Gradeck et al. [26]	$E_{1d} = \int_0^{t_R} h_{imp}\left(T_w - T_s\right)\frac{\pi d(t)^2}{4}dt + \int_0^{t_R}\epsilon_w\sigma_{SB}\left(T_w^4 - T_d^4\right)\frac{\pi d(t)^2}{4}dt$
	Owen and Hewitt (*apud* [27])	$\dot{m}_{imp,d} = \begin{cases} \frac{0.18}{\sqrt{\rho_s D_{int}/\gamma_d}}\alpha_d\rho_d & \left(\frac{\alpha_d\rho_d}{\rho_d} < 0.3\right) \\ \frac{0.083}{\sqrt{\rho_s D_{int}/\gamma_d}}\left(\alpha_d\rho_d\right)^{0.35}\rho_s^{0.65} & \left(\frac{\alpha_d\rho_d}{\rho_d} \geq 0.3\right) \end{cases}$

wall ($\Phi_{imp,wd}$). In NECTAR, we use the correlation proposed by Gradeck et al. for the energy E_{1d} extracted by the impact of a single droplet. Figure 4 shows that Gradeck et al. model estimates E_{1d} by one order higher than Guo and Mishima correlation. This might affect substantially the estimation of the total heat dissipation Φ_{int} with Eq. 3 and the contribution by each heat transfer path, especially because Guo and Mishima had already seen that $\Phi_{imp,wd}$ is not negligible [12].

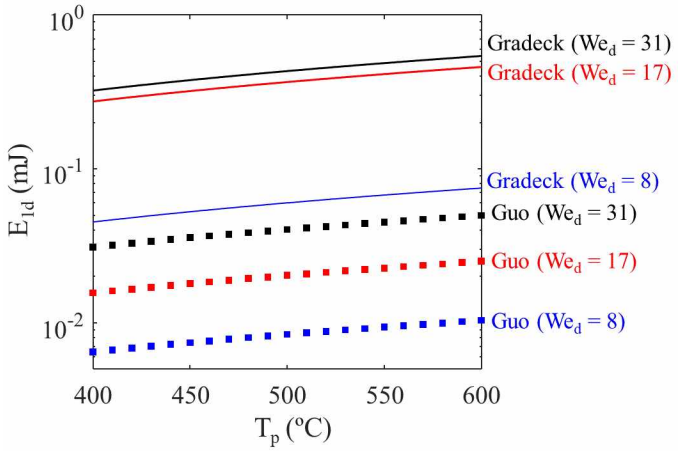

Figure 4: Comparison of Guo and Mishima [12] and Gradeck et al. [26] models for the energy extracted with the impact of one droplet as a function of the wall temperature for different Weber numbers.

As Gradeck et al. correlation estimates the heat extracted by a single droplet, we can estimate the corresponding heat flux $\varphi_{imp,wd}$ with the following equation:

$$\varphi_{imp,wd} = \frac{\dot{m}_{imp,d}}{\rho_l \pi d_d^3/6} E_{1d} \tag{9}$$

where $\dot{m}_{imp,d}$ is the mass flow rate of droplets with a diameter of d_d impinging onto the wall, for which we used the correlation proposed by Owen and Hewitt (*apud* [27]), while Guo and Mishima used either the correlation by Kataoka and Ishii and the one by Whalley and Hewitt (*apud* [12]). In the results section, we compare our approach

to Guo and Mishima's for the droplet impact heat transfer.

3.4. Transport equations for the droplets evolution

We used the following equation based on the moment density approach [28–30] to describe the volumetric evolution of the dispersed phase along the z-axis:

$$\frac{d\left[S_\eta(z)u_{d,\eta}(z)\right]}{dz} = \eta S_{\eta-1}(z)G_{\eta-1}(z) + \omega_\eta(z) \tag{10}$$

The first term in the right of Eq. 10 regards the change in the droplets volume by evaporation, while the second term (ω_η) regards the droplets coalescence and breakup, which is set as $\omega_\eta = 0$ in NECTAR. We used a different approach to consider droplets breakup in our code, which is presented in section 3.6. For S_η, $u_{d,\eta}$ and G_η, Morel et al. [29] provides the following expressions:

$$S_\eta(z) = n(z)\int_0^\infty P(d_d, z)d_d^\eta dd_d \tag{11}$$

$$u_{d,\eta}(z) = \frac{\int_0^\infty P(d_d, z)u_d(d_d, z)d_d^\eta dd_d}{\int_0^\infty P(d_d, z)d_d^\eta dd_d} \tag{12}$$

$$G_\eta(z) = \frac{\int_0^\infty P(d_d, z)\dot{G}(d_d, z)d_d^\eta dd_d}{\int_0^\infty P(d_d, z)d_d^\eta dd_d} \tag{13}$$

being $S_\eta(z)$ the moment of order η, $P(d_d, z)$ and $u_d(d_d, z)$, respectively, the droplets diameter and velocity distributions at the axial position z, and $\dot{G}(d, z)$ the distribution of the change in the droplets diameter (dd_d/dt) due to evaporation.

Finally, we obtain S_η for $\eta = 0, 1, 2, 3$ and, for any sort of distribution of the droplets diameter and velocity, we can estimate volumetric characteristics of the dispersed phase (the density of droplets n, the interfacial area concentration a_i, and the volume fraction α_d) along the z-direction with the following equations:

$$n(z) = S_0(z) \tag{14}$$

$$a_i(z) = \pi S_2(z) \tag{15}$$

$$\alpha_d(z) = \pi S_3(z)/6 \tag{16}$$

To calculate the values of S_η, we must define the droplets diameter distribution. We have already observed that the droplets diameter polydispersion can be described by a log-normal distribution (Fig. 5) [17], which is defined by the equation:

$$P(d_d, z) = \frac{1}{\sqrt{2\pi}\sigma(z)d_d}\exp\left\{-\frac{\left[\ln\left(\frac{d_d}{\mu(z)}\right)\right]^2}{2\sigma^2(z)}\right\} \tag{17}$$

where μ is the mean diameter and σ is the standard deviation of the log-normal distribution. Hence, applying Eq. 17 to Eq. 11, we find:

$$S_\eta = \frac{6\alpha_d}{\pi}\mu^{\eta-3}\exp\left[\frac{\sigma\left(\eta^2-9\right)}{2}\right] \tag{18}$$

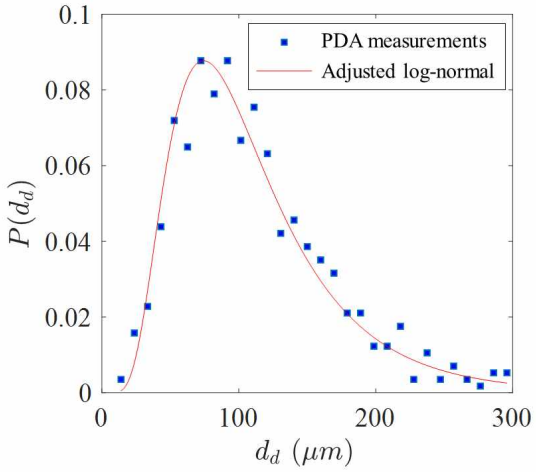

Figure 5: Log-normal distribution fitting experimental data for the droplets diameter (PDA measurements upstream of the heated tube with a not-deformed tube)

Inversely, the log-normal parameters μ and σ can be calculated with the first and second moments (S_1 and S_2):

$$\sigma = \sqrt{\ln\left(\frac{6\alpha_d S_1}{\pi S_2^2}\right)} \tag{19}$$

$$\mu = \frac{6\alpha_d}{\pi S_2}\exp\left(-\frac{5}{2}\sigma^2\right) \tag{20}$$

3.5. Discretization of the log-normal distribution

This is already evident that the mechanistic models implemented in NECTAR depends substantially on the droplets diameter distribution, either for the conservation equations and for the transport equations of the dispersed phase. One usual approach that was used, for instance, by Guo and Mishima [12] is to consider a mean diameter that is representative of all the droplets. The Sauter mean diameter d_{32} is a popular choice because it conserves the droplets mean volume-to-surface ratio. In NECTAR, we chose a more realistic approach by conserving the polydispersed nature of the droplets diameter. As done by Meholic et al. [13, 31], we divided the probability distribution into several bins, each one having a Sauter mean diameter $d_{32,j}$ calculated by:

$$d_{32,j} = \frac{\int_{d_{low,j}}^{d_{up,j}} P(d,z)d^3 dd_d}{\int_{d_{low,j}}^{d_{up,j}} P(d,z)d^2 dd_d} \tag{21}$$

being $d_{low,j}$ and $d_{up,j}$ the respective lower and upper limits of the bin j. This results in a polydispersed representation of the droplets as shown in Fig. 6.

Therefore, all the conservation equations are solved for each diameter $d_{32,j}$. Meanwhile, the total rate of heat transfer for each process (radiation, convection and droplets impact) is the summation of the contribution from

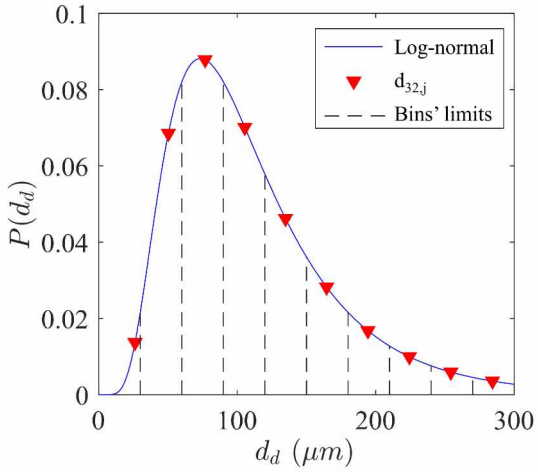

Figure 6: Discretization of the droplets diameter PDF in bins for the conservation equations.

each bin, except for the droplet evaporation (Eq. 8), which is separately evaluated for each bin, and wall-to-steam radiation, which is calculated as the mean value of the results for each bin. Therefore, we can estimate the rate of decrease in the droplet diameter dd_d/dt for each bin and, by consequence, the distribution of this change $\dot{G}$ to calculate the parameter G_η with Eq. 13. Then, the moments S_η on the next element $z + dz$ (downstream) can be calculated with Eq. 10 and, afterward, the new log-normal parameters σ and μ with Eqs. 19 and 20, respectively. The diameter log-normal distribution is finally redrawn and once again discretized. This loop continues until the last element of the domain at the outlet.

3.6. Droplets breakup

Because of the blockage in the tube and the imposed flow rate that forces all the steam to pass through the constriction (which is not true in a real nuclear reactor geometry), the relative velocity between the steam and droplets can be sufficiently high to induce hydrodynamic instabilities and, consequently, droplets breakup. This phenomenon occurs when the Weber number We_d of the droplet $d_{32,j}$ is higher than 12 [27], this number being calculated by:

$$We_{d,j} = \frac{\rho_s \left(u_s - u_{d,j}\right)^2 d_{32,j}}{\gamma_d} \tag{22}$$

where ρ_s is the steam density, u_s the steam velocity, $u_{d,j}$ the droplet velocity for the diameter class j, and γ_d the liquid surface tension. Figure 7 presents the Weber number calculated with NECTAR at the inlet of the blockage for each geometry. We can see that droplet breakup occurs only for the blockage ratio of 90%, which is in accordance with previous results [17].

Furthermore, we can affirm that the bag-breakup mode is the main fragmentation mechanism, which takes place for Weber numbers between 12 and 50 [32]. Therefore, we used the Chou and Faeth model [33] to find the child-droplets characteristics based on the diameter and volume fraction of the parent-droplet undergoing breakup. They observed that droplets generated from the bag's basal ring have a mean diameter equal to 30% of the parent-droplet's and correspond to 56% of the parent-droplet volume. Meanwhile, the other 44% of the volume, which corresponds to the bag itself, forms child-droplets with a much smaller diameter (4.2% of the parent-droplet's).

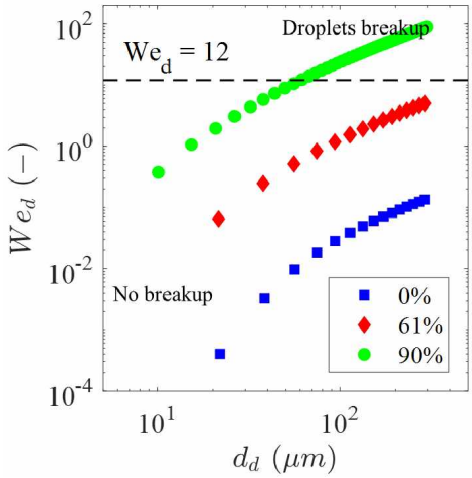

Figure 7: Droplets Weber number at the blockage in function of their respective diameter.

The application of the droplets breakup phenomenon into NECTAR is performed by calculating the Weber number with Eq. 22 for each droplet diameter $d_{32,j}$ and at each position z of the tube. If the Weber number is higher than 12, the model by Chou and Faeth is applied to the corresponding droplet and its child-droplets are added to the droplets distribution before the breakup. Afterward, we find new log-normal distribution by calculating the parameters σ and μ with the child-droplets and the droplets that did not undergo breakup, and limiting the maximum droplets diameter to a value that provides $We_d = 12$. Figure 8 presents the droplets diameter distribution after breakup compared to the condition before breakup for the case of 90% blockage ratio. Also, the breakup time is not considered in NECTAR because its duration is negligible compared to the droplets dynamics. In other words, the displacement of the droplets is very short during the breakup period.

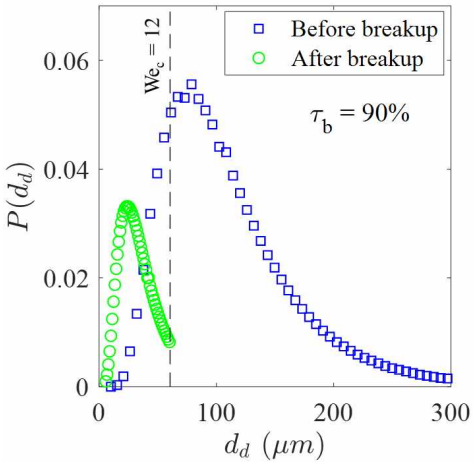

Figure 8: Distributions before and after droplets breakup taking place with the 90% blockage ratio configuration.

If we compare the current modeling with the well-known MUSIG model [34], we notice that both of them conserves the polydispersed distribution of the droplets diameter by discretizing it in bins. Nevertheless, regarding the modeling of droplets breakup, MUSIG and NECTAR use different approaches. The first uses sources and sinks in continuity equations for each bin to respect mass balance during droplets breakup and coalescence. The latter, in

its turn, reconstructs the polydispersed distribution in the event of droplets breakup, redefines the bins' limits and recalculates their respective Sauter mean diameters. Besides, no droplets coalescence is considered in NECTAR.

3.7. Implementation of NECTAR

The simulation domain of NECTAR is restricted to Part II of the test section, which means the tube between the two optical windows with length L_t (Fig. 2). The geometrical characteristics of each configuration (Table 1) are properly modeled during the 1-D discretization in the z-direction (axial), including the convergent and divergent parts found in configurations 2 and 3. The length of the domain contains N elements with a height dz to solve the conservation equations for each element.

The main outputs of NECTAR are the total heat dissipation by the internal two-phase flow, found by evaluating each heat transfer path, and the thermal-hydraulic characteristics of both the steam and the droplets. We used several experimental data from COLIBRI as boundary conditions in NECTAR so we can appropriately validate the code by comparing the experimental and simulation results (Fig. 9).

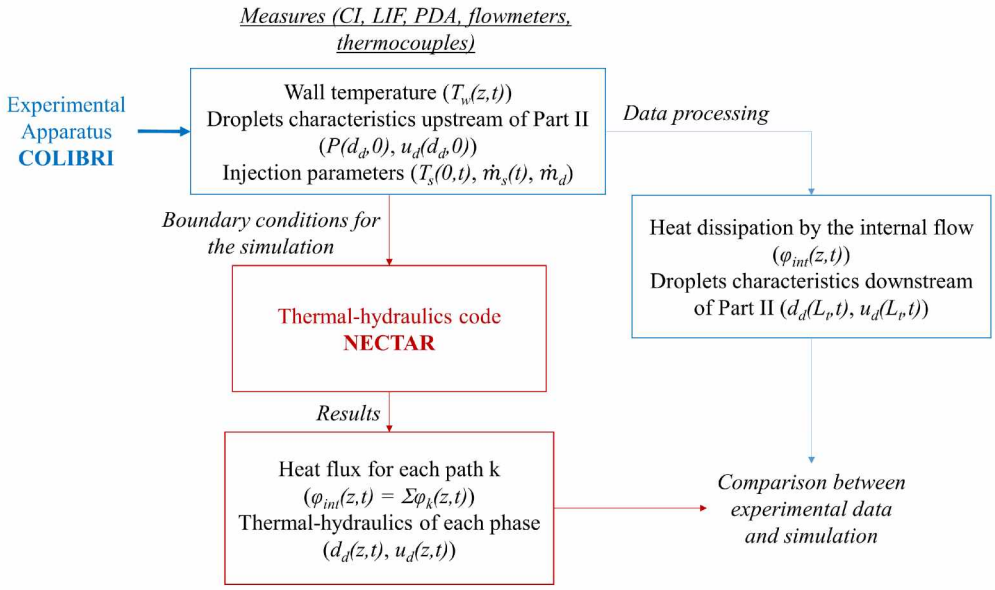

Figure 9: Flowchart of the simulation with NECTAR and comparison with experimental data from COLIBRI.

These conditions are the following:

- The wall temperature profile in the z-direction obtained with IRT at each instant ($T_w(z,t)$);
- The steam and droplets mass flow rates. The steam velocity at the inlet of the domain is estimated with the temporal flowmeter measurements and considering uniform profile ($u_s(t) = 4\dot{m}_s(t)/(\pi\rho_s D_{int}^2)$). The droplets velocity at the inlet $u_d(d_d,0)$ is the mean velocity measured with the PDA upstream of Part II. Also, it is set as constant throughout the cooling phase and the same for all droplets diameters;
- The droplets diameter distribution at the inlet ($P(d_d,0)$) is a log-normal distribution representative of the PDA results upstream of Part II and is constant throughout the cooling phase;

- As already mentioned in the hypotheses, the droplets at the inlet are at the saturation temperature. Meanwhile, the steam temperature at the inlet $T_s(0,t)$ is the one measured upstream of Part II by a thermocouple.

4. Results and discussion

4.1. Preliminary validation with monophasic steam flow

Since there are many heat transfer paths in the two-phase flow and several empirical correlations involved in the problem, we performed a first validation with a monophasic flow of steam to validate the choice of the Gnielinski correlation for the wall-to-steam convection ($\Phi_{c,ws}$ in Table 3). This is an important step for the validation of NECTAR because it is expected that this heat transfer path plays a major role in the overall heat dissipation. An inappropriate correlation for $\Phi_{c,ws}$ could affect significantly the model accuracy or mislead the interpretation of the contribution by each heat transfer path.

We performed the test with the three configurations shown in Table 1 applying similar boundary conditions (Table 4).

Table 4: Mean values of the steam flow rate and temperature at the inlet and the initial mean temperature of the tube (monophasic flow).

Config.	τ_b	$\widetilde{\dot{m}}_s$	$\widetilde{T}_s(z=0)$	$\overline{T}_w(t=0)$
1	0%	4.47 kg/h	162 °C	603 °C
2	61%	4.44 kg/h	165 °C	567 °C
3	90%	4.22 kg/h	160 °C	542 °C

As the experiments involve tubes with different diameters D_{int}, the heat transfer per unit length Φ_{int}/L_b was used to better compare the results:

$$\frac{\Phi_{int}}{L_b} = \pi D_{int} \varphi_{int} \tag{23}$$

where φ_{int} is the total heat flux dissipated by the internal flow. We remind that the experimental value of φ_{int} is obtained with Eq. 2.

Figure 10 presents the comparison of NECTAR and DRACCAR calculations and experimental data for the variation in $\widetilde{\Phi}_{int}/L_b$ with the wall temperature $\widetilde{T}_w$. The tilde over these parameters indicates mean values that were calculated by collecting points of T_w and their respective Φ_{int}/L_b throughout the cooling phase. More precisely, by grouping data within ranges of 10 °C in the wall temperature, we calculate the mean values $\widetilde{T}_w$ and $\widetilde{\Phi}_{int}/L_b$ and plot mean boiling curves as we present in Fig 10. Both codes predict with great accuracy the heat dissipation by the internal flow.

In this case of monophasic steam flow, the heat transfer paths are only convection and radiation from wall to steam ($\Phi_{c,ws}$ and $\Phi_{r,ws}$, respectively). According to the NECTAR results, $\Phi_{c,ws}$ is responsible for more than 95% of the heat dissipation in all the three cases. Therefore, by considering that NECTAR predictions for the heat dissipation by the internal flow fall within the experimental uncertainty and within the range of ±20% deviation (Fig. 11a),

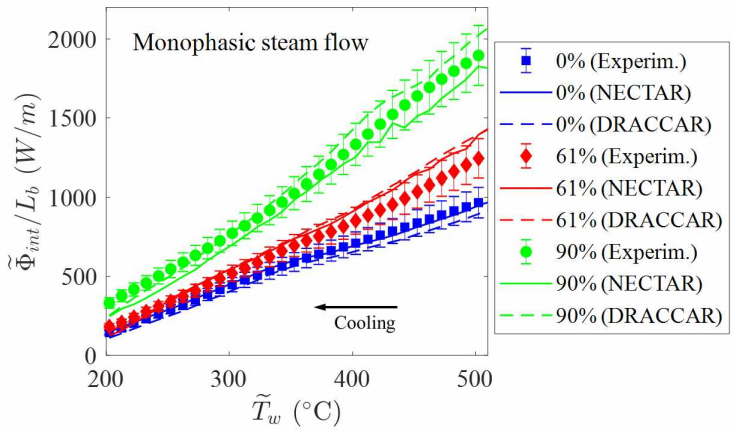

Figure 10: Average values of heat transfer per unit length with the wall temperature for each configuration with monophasic flow: comparison of experimental data and calculations using NECTAR and IRSN's code DRACCAR.

we validate the use of Gnielinski correlation in NECTAR to estimate $\Phi_{c,ws}$. Similarly, DRACCAR correlations for monophasic flows are also appropriate (Fig. 11b), especially concerning wall-to-steam convective heat transfer.

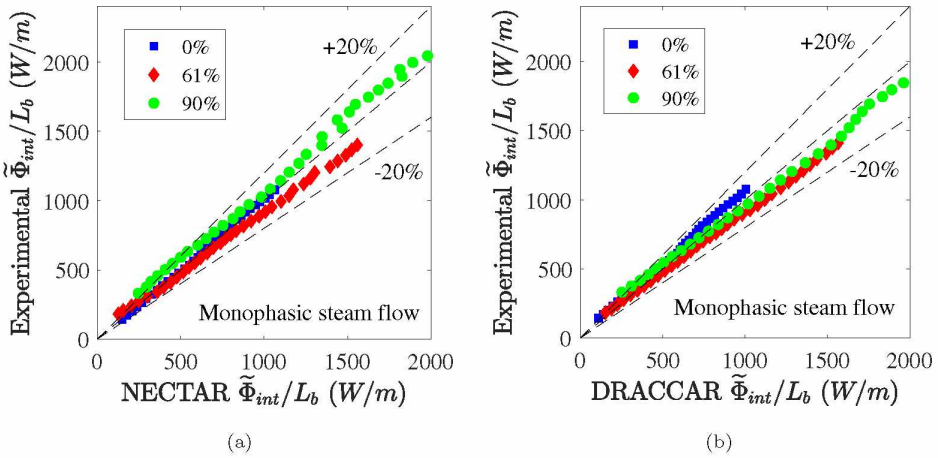

Figure 11: Comparison of experimental data and code calculations for Φ_{int}/L_b with monophasic flow. (a) NECTAR; (b) DRACCAR.

4.2. Validation with two-phase flow

Table 5 presents the boundary conditions of each tested case, while Fig. 12 presents PDA measurements of the droplets diameter distribution and droplets velocity-diameter correlation upstream of Part II for each configuration. These results are important to ensure that all the cases have similar inlet and initial conditions, which allow us to analyze only the blockage ratio effect on the heat transfer processes and the droplets dynamics. In this section, we validate the code NECTAR with an internal steam-droplets two-phase flow, first by estimating the heat dissipation (subsection 4.2.1) and then by calculating the droplets velocity as a function their diameter (subsection 4.2.2). All these calculations were performed using 15 bins in the discretization of the droplets diameter distribution, except for the case of 90% blockage ratio where we used 50 bins because of the occurrence of droplets breakup.

Table 5: Mean values of the steam and droplets characteristics at the inlet and the initial tube temperature (two-phase flow).

Config.	τ_b	$\widetilde{\dot{m}}_s$	$\widetilde{T}_s(z=0)$	$\dot{m}_d$	$\widetilde{u}_d(z=0)$	$d_d(z=0)$	$\overline{T}_w(t=0)$
1	0%	4.40 kg/h	168 °C	0.8 kg/h	16.0 m/s	110 μm	641 °C
2	61%	4.39 kg/h	170 °C		14.8 m/s	86 μm	657 °C
3	90%	4.10 kg/h	168 °C		13.0 m/s	98 μm	583 °C

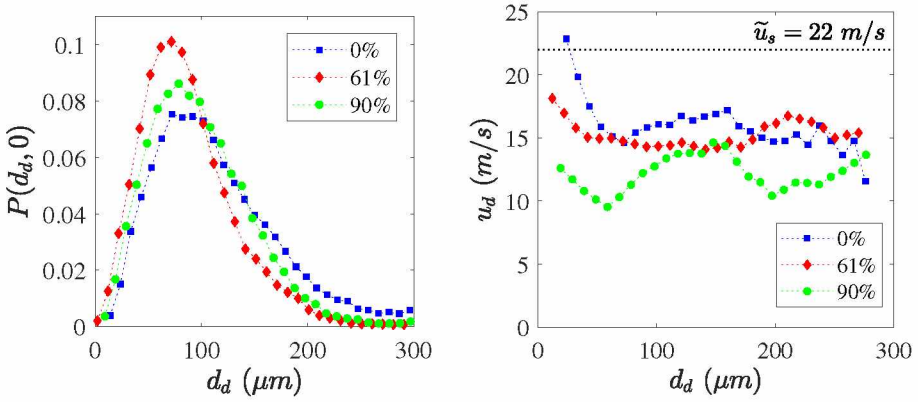

Figure 12: Experimental results for the droplets dynamics upstream of the test section: (a) droplet diameter distribution of droplets; (b) axial droplet velocity as a function of a droplet diameter.

4.2.1. Heat dissipation by the internal flow

As we mentioned in the hypotheses made for NECTAR, the code is only valid during the Leidenfrost regime. This statement is evident when we look at the mean boiling curve in Fig. 13. The code no longer represents well experimental data after the wall rewetting, i.e. for temperatures lower than the Leidenfrost point (at the minimal rate of heat flow). Therefore, all the results concerning NECTAR, and its comparison with experimental data, are herein discussed only in the Leidenfrost regime.

Figure 14 compares boiling curves obtained by measurements and by simulations (NECTAR and DRACCAR) for each configuration. In the case of two-phase flow, more heat transfer paths are involved during the cooling phase ($\Phi_{imp,wd}$, $\Phi_{r,wd}$, $\Phi_{c,sd}$, $\Phi_{r,sd}$) as well as droplet evaporation ($\dot{m}_e$). NECTAR still predicts with great accuracy the dissipated heat, most of the estimated values being within the error bars. Moreover, 99% of NECTAR results diverge less than 20% from experimental data, resulting in a mean absolute deviation less than 8% for all the configurations (Fig. 15a). Regarding DRACCAR results, we can see in Fig. 15b great match between calculations and experimental results for the case with 90% blockage ratio, but not so accurate for the 0% configuration. As we discuss further the contribution by each heat transfer path, droplets impact plays an important role in the internal heat dissipation for the case of 0% blockage ratio. Since DRACCAR does not consider this phenomenon in the calculations, it estimates lower rates of heat transfer compared to experimental data. On the other hand, this difference between experimental and simulation is almost inexistent for 90% blockage ratio because wall-to-steam convection is responsible for almost the entire heat dissipation and, hence, droplets impact has little importance in this case.

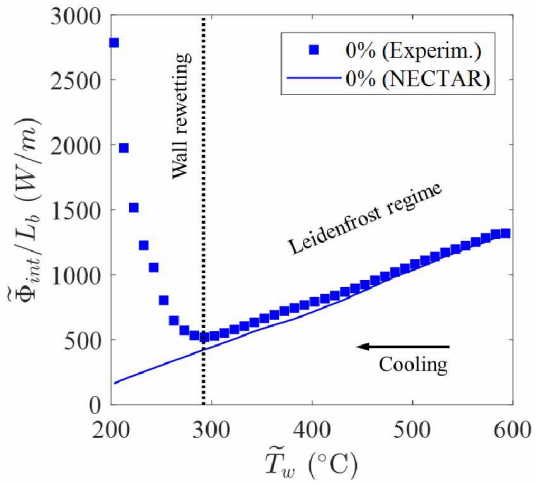

Figure 13: Code validity example with a two-phase steam-droplets flow and 0% blockage ratio.

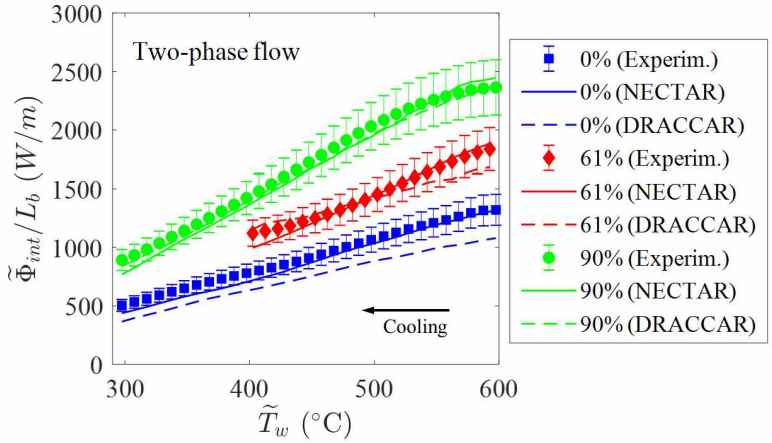

Figure 14: Average values of heat transfer per unit length with the wall temperature for each configuration with steam-droplets two-phase flow: comparison of experimental data and calculations using NECTAR and IRSN's code DRACCAR.

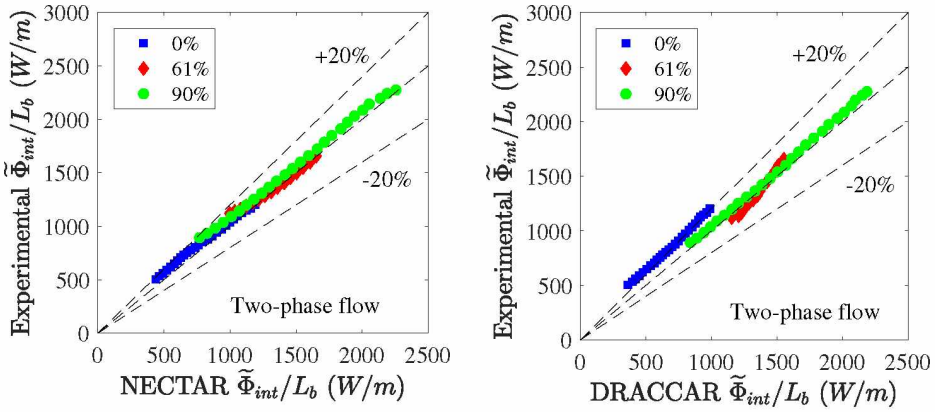

(a) (b)

Figure 15: Comparison of experimental data and code calculations for Φ_{int}/L_b with steam-droplets two-phase flow. (a) NECTAR; (b) DRACCAR.

As we mentioned in section 3.3, we used Gradeck et al and Owen and Hewitt correlations to estimate $\Phi_{imp,wd}$ instead of using the model by Guo and Mishima. Figure 16 compares NECTAR results using each of these models with experimental data. The results using Gradeck et al model presents great fit with experiments, while Guo and Mishima model underestimates the internal heat dissipation. This is because Gradeck et al correlation estimates higher heat removal by droplets impact compared to Guo and Mishima's, as shown in Fig. 4. Therefore, the other correlations used in NECTAR apart from Gnielinki's correlation are also appropriate to describe COLIBRI experimental results.

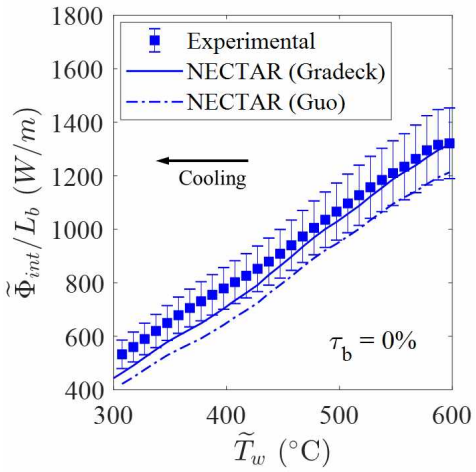

Figure 16: Comparison between experimental data for 0% blockage ratio and NECTAR calculations using Gradeck et al or Guo and Mishima correlations to estimate $\Phi_{imp,wd}$.

4.2.2. Droplets dynamics

The second part of the code validation is to compare the calculated droplets velocity downstream of Part II with experimental results. We focus this analysis only to NECTAR because the polydispersion discretization allows us to analyze the droplets velocity-diameter correlation. As depicted in Fig. 17, NECTAR predicts well the droplets velocity along the cooling phase for all the configurations. Nevertheless, there are two punctual exceptions: the velocity of the smallest and the largest droplets at the end of the cooling phase for 0% blockage ratio and the velocity of larger droplets for 90% blockage ratio within the periods between 4 s and 8 s and between 16 s and 20 s. The latter is apparently a particularity of the experimental result between 4 s and 8 s as this is the only shape of the droplets diameter-velocity correlation (parabolic) that does not follow the other trends (increasing velocity for larger droplets). Because droplets breakup takes place for 90% blockage ratio, we only find droplets smaller than about 60 μm, which is well predicted by NECTAR.

This is interesting to notice that the shape of the velocity-diameter curves in Fig. 17 are different for each geometry. This happens because of the Venturi effect that accelerates the steam and, by drag force, the droplets. Because of their lower inertia, smaller droplets are more easily accelerated than the larger ones. For the case of 0% blockage ratio, there is no Venturi effect but there is an acceleration of the steam due to heating. For this reason, the droplets velocity decreases with the increasing diameter in this configuration. However, for the cases of 61% and 90% blockage ratio, the droplets are at first accelerated in the blockage and later slowed down in the expansion downstream of the blockage. Hence, the smallest droplets rapidly follow the steam flow and their velocity is substantially reduced.

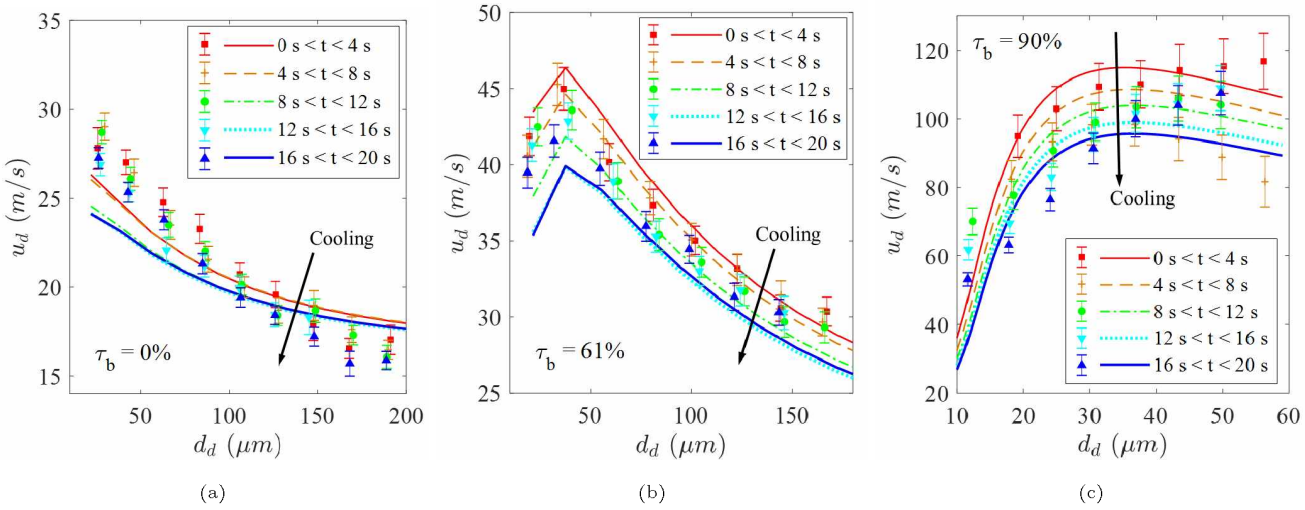

Figure 17: Droplets diameter-velocity correlation for each time period of the cooling phase (markers are experimental results; lines are NECTAR results) and for each blockage ratio: a) 0%; b) 61%; and c) 90%.

Larger droplets have higher inertia and, consequently, their velocity is less affected. That is the reason why we see a velocity peak for 61% blockage ratio at about $d_d = 30\mu m$ and an increasing trend for 90% blockage ratio, where we have only small droplets due to the breakup.

4.3. Contribution by each heat transfer path to the internal heat dissipation

Since NECTAR has been validated in both the heat transfer aspects and the droplets dynamics, we can evaluate in detail the thermal-hydraulics of the flow, as well as the contributions by each heat transfer path described in Fig. 3. In this section, we evaluate the role of each heat transfer process in the internal heat dissipation, while in the next section we present a similar analysis for the droplets evaporation process.

Table 6 presents the contribution by each heat transfer path to the heat dissipation by the internal steam-droplets flow. These values are averaged for wall temperatures between 400 °C and 550 °C. Wall-to-steam forced convection plays a major role in the cooling, corresponding to more than 87% of the total heat dissipation. Furthermore, because of the Venturi effect and the imposed flow of steam, the contribution of this phenomenon increases with the increasing blockage ratio, being basically responsible for all the internal heat dissipation for the configuration with the 90% blockage ratio.

Even though the volume fraction of the dispersed flow is very low in the present study (about 10^{-4}), the heat removed by the droplets impact has substantial participation in the heat dissipation, especially for the case with 0% blockage ratio. As mentioned before, Guo and Mishima had already observed that the heat transfer due to droplets impact is not negligible. NECTAR results using Gradeck et al correlation shows that not only this heat transfer path is not negligible but also this is the second most important heat transfer path of the cooling.

Finally, radiation plays a minor role in the heat dissipation in the present cases. For a blockage ratio of 0%, wall-to-steam radiation still has a little participation of about 4%. Nevertheless, this is easily negligible in the other configurations. Wall-to-droplets radiation, in its turn, is always negligible as this heat transfer path never contributes by more than 1% to the heat dissipation. This is a consequence of the very low volume fraction of droplets in the experiments.

Table 6: Average contribution by each heat transfer path to the internal heat dissipation for each configuration ($400\,^{\circ}\mathrm{C} \leq T_w \leq 550\,^{\circ}\mathrm{C}$).

Heat dissipation	$\tau_b = 0\%$	$\tau_b = 61\%$	$\tau_b = 90\%$
$\widetilde{\Phi}_{c,ws}$	87.7%	92.1%	97.2%
$\widetilde{\Phi}_{imp,wd}$	8.1%	6.1%	2.2%
$\widetilde{\Phi}_{r,ws}$	3.7%	1.5%	0.4%
$\widetilde{\Phi}_{r,wd}$	0.5%	0.3%	0.2%
$\widetilde{\Phi}_{int}$ (Summation)	100%	100%	100%

4.4. Contribution by each heat transfer path to the droplets evaporation

Figure 18 presents the fraction of the droplets mass that evaporates after passing through the heated tube. As expected, the droplets evaporation rate decreases with lower wall temperatures. We found similar values of evaporated mass with the 0% and 61% blockage ratio configurations. However, we can observe a substantial increase in the evaporated mass for 90% blockage ratio because of the Venturi effect together with the droplets breakup that increases substantially the droplets surface-to-volume ratio. This means steam-to-droplets convection is enhanced, leading to higher rates of evaporation.

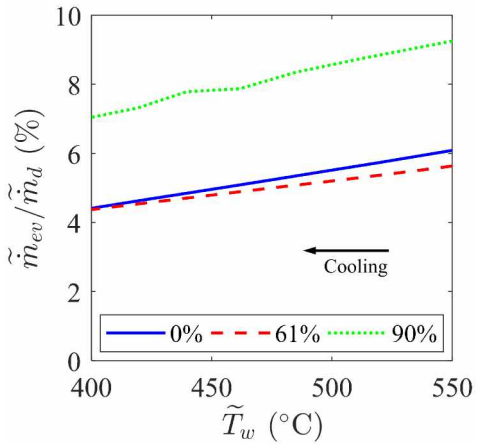

Figure 18: Relative evaporated mass of droplets in function of the wall temperature for each configuration.

This analysis is confirmed when looking at Table 7 that presents the average contribution by each heat transfer path to the droplets evaporation ($400\,^{\circ}\mathrm{C} \leq T_w \leq 550\,^{\circ}\mathrm{C}$). For all the cases, droplets impact onto the wall plays an important role on the droplets evaporation, corresponding to nearly 60% for the cases with 0% and 61% blockage ratio and to 40% for the configuration with 90% blockage ratio. Steam-to-droplets convection is the other heat transfer path having significant contribution. This happens especially for the case of 90% blockage ratio because of droplets break-up and the acceleration of the steam phase due to the Venturi effect. Next, there is a small contribution of 3% to 4% by the wall-to-droplets radiative heat transfer. Finally, steam-to-droplets radiation is practically zero and can easily be neglected for the tested cases.

Table 7: Average contribution by each heat transfer path to the droplets evaporation for each configuration (400 °C $\leq T_w \leq$ 550 °C).

Droplet evaporation	$\tau_b = 0\%$	$\tau_b = 61\%$	$\tau_b = 90\%$
$\widetilde{\Phi}_{imp,wd}$	63.6%	57.3%	40.0%
$\widetilde{\Phi}_{c,sd}$	32.2%	39.5%	56.7%
$\widetilde{\Phi}_{r,wd}$	4.2%	3.2%	3.3%
$\widetilde{\Phi}_{r,sd}$	$\approx 0\%$	$\approx 0\%$	$\approx 0\%$
$\widetilde{\Phi}_{ev}$ (Summation)	100%	100%	100%

4.5. Analysis of the droplets diameter discretization

As mentioned before, one of the NECTAR's capabilities is considering the polydispersion of the droplets diameter. The major advantage of this feature is to better describe the real condition of the flow compared to using a single droplet diameter to represent the whole droplets population. Unfortunately, the computational cost increases as long as we increase the number of bins in the droplets diameter discretization.

To highlight the importance of preserving the polydispersion, Fig.19 presents NECTAR results of the estimated internal heat dissipation with the 0% blockage ratio geometry for two different flow conditions and using different number of bins N_{bins} in the discretization. The first analysis (Fig. 19a) regards the same flow conditions of the Table 5, which results in the already mentioned very low volume fraction of droplets ($\alpha_d \approx 1.10^{-4}$). In the second analysis (Fig. 19b), we use different values of droplets and steam mass flows and steam temperature ($\dot{m}_d = 40$ kg/h, $\widetilde{\dot{m}}_s = 2.64$ kg/h, and $\widetilde{T}_s(z=0) = 288\,^{\circ}$C, respectively) and kept the same values for the others. This results in an increase in the volume fraction of droplets to approximately 7.10^{-3} and a decrease in the contribution of wall-to-steam convection. These values used in the second analysis still comply with typical LOCA conditions [6, 7, 21].

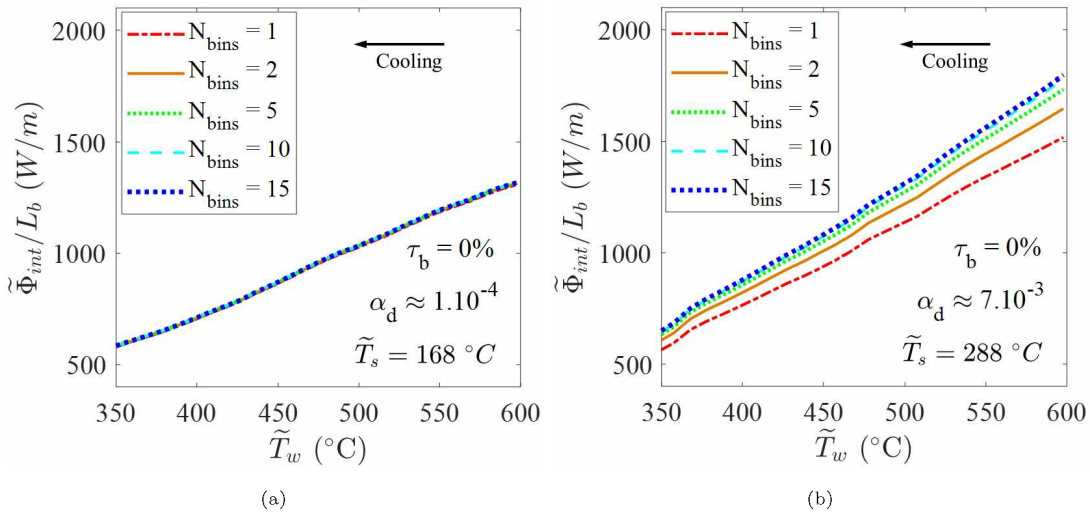

Figure 19: NECTAR results for 0% blockage ratio using different number of bins in the droplets diameter distribution: a) scenario with lower volume fraction of droplets and lower steam temperature; b) scenario with higher volume fraction of droplets and higher steam temperature.

Figure 19a shows that NECTAR calculations with 1 bin and 15 bins are virtually the same, so there is no advantage in using the polydispersed distribution to estimate the internal heat dissipation with low volume fraction scenario. In contrast, the polydispersion discretization becomes important in the second case with high volume fraction and higher steam temperature (Figure 19b). For instance, the mean difference between the estimated internal heat dissipation using 1 and 15 bins is about 14%. Indeed, this is related to the more important role played by the droplets in the second case. Direct impact of droplets and wall-to-droplets radiation, for example, correspond respectively to 22.4% and 23.8% of the internal heat dissipation in the second scenario, while in the first they contribute to only 8.1% and 0.5% (Table 6). Meanwhile, the contribution by wall-to-steam convection decreases from 87.7% to 50.8%. Hence, keeping the polydispersion distribution of the droplets diameter is important when the droplets contribution to the thermal-hydraulics of the flow is more significant.

5. Conclusions

The present work introduces a new code named NECTAR to estimate the heat dissipation by an internal polydispersed flow film boiling in LOCA conditions at sub-channel scale. The simulation results are compared with experiments performed with the test apparatus COLIBRI, which was specially built to provide data to validate thermal-hydraulics mechanistic models. NECTAR considers six heat transfer paths between wall, steam and droplets, as well as mass transfer due to droplets evaporation. Furthermore, NECTAR uses different correlations from the model by Guo and Mishima and considers a polydispersed distribution of the droplets diameter and droplets breakup. The main findings of this work are:

- NECTAR predicts with great accuracy the heat dissipation by an internal steam-droplets two-phase flow, with a mean deviation of less than 8% from experimental data, which indicates that all the chosen correlations are appropriate to describe the heat transfer exchanges;
- NECTAR also predicts well the droplets velocity downstream of the heated tube in function of the droplets diameter;
- Because of the very low volume fraction of droplets in the test cases (about 10^{-4}) and the imposed flow of steam to the blockage, wall-to-steam convective heat transfer plays the major role among the heat transfer paths. It corresponds to approximately 90% of the internal heat dissipation for the cases of 0% and 61% blockage ratio and to 97% of the heat dissipation for 90% blockage ratio;
- Despite the very low volume fraction of droplets in the flow, droplets impact onto the heated wall has substantial participation in the heat removal and cannot be neglected in thermal-hydraulics calculations;
- Moreover, droplets impact and steam-to-droplets convection are responsible for more than 95% of the heat targeted to the droplets evaporation;
- Finally, because of the low volume fraction of droplets and the large contribution by the wall-to-steam convective heat transfer, the discretization of the droplets diameters did not affect NECTAR calculations for the heat dissipation. Nevertheless, in a simulation with high volume fraction and a higher steam temperature

(hence lower contribution by the wall-to-steam convection), the polydispersed distribution approach provides significantly different results compared to the monodisperse diameter calculations.

The present findings are important for the improvement of computational codes by analyzing important features to be considered in mechanistic modeling. For instance, it is intended to implement in IRSN's code DRACCAR the equations used in NECTAR for heat dissipation by droplets impact, which might serve as well for others like CATHARE and TRACE. In a further work, the implementation of the diameter polydispersed distribution is also desired, although this step must still be validated with more experimental data with higher droplets volume fractions.

6. Acknowledgments

This work is completed within the framework of RSNR Project PERFROI from a French State aid managed by the French National Research Agency under the program of Investments for the Future carrying the reference n° ANR-11-RSNR-0017.

References

[1] C.-H. Song, Some issues and challenges in advanced thermal-hydraulic safety research, Nuclear Technology 196 (3) (2016) 421–445. doi:https://doi.org/10.13182/NT16-91.

[2] T. Glantz, T. Taurines, S. Belon, O. D. Luze, G. Guillard, F. Jacq, Draccar: A multi-physics code for computational analysis of multi-rod ballooning, coolability and fuel relocation during loca transients. part two: Overview of modeling capabilities for loca, Nuclear Engineering and Design 339 (2018) 202 – 214. doi:https://doi.org/10.1016/j.nucengdes.2018.08.031.

[3] T. Glantz, T. Taurines, O. D. Luze, S. Belon, G. Guillard, F. Jacq, Draccar: A multi-physics code for computational analysis of multi-rod ballooning, coolability and fuel relocation during loca transients. part one: General modeling description, Nuclear Engineering and Design 339 (2018) 269 – 285. doi:https://doi.org/10.1016/j.nucengdes.2018.06.022.

[4] Y. Jin, F. R. Beck, B. R. Lowery, D. J. Miller, F. B. Cheung, S. M. Bajorek, K. Tien, C. L. Hoxie, Experimental study of droplet sizes across a spacer grid location under various reflood conditions, Experimental Thermal and Fluid Science 94 (February 2017) (2018) 246–257. doi:https://doi.org/10.1016/j.expthermflusci.2018.02.017.

[5] Z. Hózer, I. Nagy, M. Kunstár, P. Szabó, N. Vér, R. Farkas, I. Trosztel, A. Vimi, Experimental investigation of the coolability of blocked hexagonal bundles, Nuclear Engineering and Design 317 (2017) 51 – 58. doi:https://doi.org/10.1016/j.nucengdes.2017.03.030.

[6] P. Ruyer, N. Seiler, B. Biton, F. Lelong, F. Secondi, D. Baalbaki, M. Gradeck, Two-phase flow across a partially damaged core during the reflood phase of a loca, Nuclear Engineering and Design 264 (2013) 187 – 194, sI:NURETH-14. doi:https://doi.org/10.1016/j.nucengdes.2013.02.026.

[7] K. Kim, B. J. Kim, H. S. Choi, S. K. Moon, C. H. Song, Effect of a blockage length on the coolability during reflood in a 2 x 2 rod bundle with a 90% partially blocked region, Nuclear Engineering and Design 312 (2017) 248–255. doi:https://doi.org/10.1016/j.nucengdes.2016.08.031.

[8] H. K. Cho, K. Y. Choi, S. Cho, C.-H. Song, Experimental observation of the droplet size change across a wet grid spacer in a 6x6 rod bundle, Nuclear Engineering and Design 241 (12) (2011) 4649 – 4656, the 18th International Conference on Nuclear Engineering (ICONE-18). doi:https://doi.org/10.1016/j.nucengdes.2011.03.042.

[9] Y. Jin, F.-B. Cheung, S. M. Bajorek, K. Tien, C. L. Hoxie, Investigation of the thermal-hydraulic non-equilibrium in a 7x7 rod bundle during reflood, International Journal of Heat and Mass Transfer 127 (2018) 266 – 279. doi:https://doi.org/10.1016/j.ijheatmasstransfer.2018.08.011.

[10] USNRC, Compendium of ECCS research for realistic LOCA analysis, NUREG-1230, Tech. rep., US Nuclear Regulatory Commission, Washington, DC (1988).

[11] K. H. Sun, J. M. Gonzales-Santalo, C. L. Tien, Calculation of Combined Radiation and Convection Heat Transfer in Rod Bundles Under Emergency Cooling Conditions, Journal of Heat Transfer 98 (3) (1976) 414–420. doi:https://doi.org/10.1115/1.3450569.

[12] Y. Guo, K. Mishima, A non-equilibrium mechanistic heat transfer model for post-dryout dispersed flow regime, Experimental Thermal and Fluid Science 26 (6-7) (2002) 861–869. doi:https://doi.org/10.1016/S0894-1777(02)00195-4.

[13] M. J. Meholic, D. L. Aumiller, F. B. Cheung, A comprehensive, mechanistic heat transfer modeling package for dispersed flow film boiling - Part 1 - Development, Nuclear Engineering and Design 291 (2015) 295–301. doi:https://doi.org/10.1016/j.nucengdes.2015.07.013.

[14] Y.-J. Wang, C. Pan, A one-dimensional semi-empirical model considering transition boiling effect for dispersed flow film boiling, Nuclear Engineering and Design 316 (2017) 99 – 111. doi:https://doi.org/10.1016/j.nucengdes.2017.03.004.

[15] H. Anglart, H. Li, G. Niewinski, Mechanistic modelling of dryout and post-dryout heat transfer, Energy 161 (2018) 352 – 360. doi:https://doi.org/10.1016/j.energy.2018.07.011.

[16] G. Repetto, C. Dominguez, B. Durville, S. Carnemolla, D. Campello, C. Tardif, M. Gradeck, The R&D PERFROI project on thermal mechanical and thermal hydraulics behaviors of a fuel rod assembly during a loss of coolant accident, International Topical Meeting on Nuclear Reactor Thermal Hydraulics 2015, NURETH 2015 1 (2015) 1–14.

[17] J. D. Peña Carrillo, A. V. S. Oliveira, A. Labergue, T. Glantz, M. Gradeck, Experimental thermal hydraulics study of the blockage ratio effect during the cooling of a vertical tube with an internal steam-droplets flow, International Journal of Heat and Mass Transfer 140 (2019) 648 – 659. doi:https://doi.org/10.1016/j.ijheatmasstransfer.2019.06.012.

[18] J. D. Peña Carrillo, Étude expérimentale du transfert paroi/fluide dans le cas d'un écoulement vertical vapeur/gouttes dans une géométrie tubulaire, Ph.D. thesis, Université de Lorraine (2018).
URL https://tel.archives-ouvertes.fr/tel-01984680

[19] A. Labergue, A. Delconte, G. Castanet, F. Lemoine, Study of the droplet size effect coupled with the laser light scattering in sprays for two-color lif thermometry measurements, Experiments in Fluids 52 (5) (2012) 1121–1132. doi:https://doi.org/10.1007/s00348-011-1242-8.

[20] C. Grandjean, Coolability of blocked regions in a rod bundle after ballooning under LOCA conditions: Main findings from a review of past experimental programmes, Nuclear Engineering and Design 237 (15) (2007) 1872 – 1886. doi:https://doi.org/10.1016/j.nucengdes.2007.02.022.

[21] R. Lee, J. Reyes, K. Almenas, Size and number density change of droplet populations above a quench front during reflood, International Journal of Heat and Mass Transfer 27 (4) (1984) 573 – 585. doi:https://doi.org/10.1016/0017-9310(84)90030-9.

[22] B. Oesterlé, Écoulements multiphasiques : des fondements aux méthodes d'ingénierie, Lavoisier, 2006.

[23] M. Yuen, L. Chen, Heat-transfer measurements of evaporating liquid droplets, International Journal of Heat and Mass Transfer 21 (5) (1978) 537 – 542. doi:https://doi.org/10.1016/0017-9310(78)90049-2.

[24] V. Gnielinski, New equations for heat and mass transfer in the turbulent flow in pipes and channels, International Chemical Engineering 16 (2) (1976) 359 – 368.

[25] K. Lee, D. J. Ryley, The evaporation of water droplets in superheated steam, Journal of Heat Transfer 90 (4) (1968) 445 – 451. doi:https://doi.org/10.1115/1.3597540.

[26] M. Gradeck, N. Seiler, P. Ruyer, D. Maillet, Heat transfer for leidenfrost drops bouncing onto a hot surface, Experimental Thermal and Fluid Science 47 (2013) 14 – 25. doi:https://doi.org/10.1016/j.expthermflusci.2012.10.023.

[27] N. I. Kolev, Multiphase Flow Dynamics, 4th Edition, Vol. 2, Springer, Berlin, 2011.

[28] P. Ruyer, Modélisation de la polydispersion en taille : Méthode des moments appliquée aux écoulements adiabatiques à bulles, Technical report, IRSN (2008).

[29] C. Morel, P. Ruyer, N. Seiler, J. M. Laviéville, Comparison of several models for multi-size bubbly flows on an adiabatic experiment, International Journal of Multiphase Flow 36 (1) (2010) 25 – 39. doi:https://doi.org/10.1016/j.ijmultiphaseflow.2009.09.003.

[30] C. Morel, Mathematical Modeling of Disperse Two-Phase Flows, Vol. 114, Springer International Publishing, 2015. doi:https://doi.org/10.1007/978-3-319-20104-7.

[31] M. J. Meholic, D. L. Aumiller, F. B. Cheung, A comprehensive, mechanistic heat transfer modeling package for dispersed flow film boiling - part 2 - implementation and assessment, Nuclear Engineering and Design 291 (2015) 302–311. doi:https://doi.org/10.1016/j.nucengdes.2015.07.014.

[32] M. Pilch, C. Erdman, Use of breakup time data and velocity history data to predict the maximum size of stable fragments for acceleration-induced breakup of a liquid drop, International Journal of Multiphase Flow 13 (6) (1987) 741 – 757. doi:https://doi.org/10.1016/0301-9322(87)90063-2.

[33] W.-H. Chou, G. Faeth, Temporal properties of secondary drop breakup in the bag breakup regime, International Journal of Multiphase Flow 24 (6) (1998) 889 – 912. doi:https://doi.org/10.1016/S0301-9322(98)00015-9.

[34] E. Krepper, D. Lucas, T. Frank, H.-M. Prasser, P. J. Zwart, The inhomogeneous musig model for the simulation of polydispersed flows, Nuclear Engineering and Design 238 (7) (2008) 1690 – 1702. doi:https://doi.org/10.1016/j.nucengdes.2008.01.004.